CrystEngComm

Accepted Manuscript

ROYAL SOCIETY OF CHEMISTRY

www.rsc.org/crystengcomm

Vertically Standing MoS_2/MoO_x Heterojunction Nanosheets for Enhanced Visible-Light Photocatalytic Active and Photostability

Gang Zhou,[a] Xiaoyong Xu, *[ab] Jianyu Yu,[a] Bin Feng,[a] Yu Zhang,[a] Jingguo Hu*[a] and Yuxue Zhou[a]

[a]*College of Physics Science and Technology, Yangzhou University, Yangzhou 225002, China*

[b]*State Key Laboratory of Bioelectronics and School of Electronic Science and Engineering, Southeast University, Nanjing 210096, China*

Abstract

The vertically aligned nanosheet heterostructures with partly reduced MoO_3 cores and adjustable MoS_2 shells were fabricated via two–step chemical vapor deposition (CVD). The as–synthesized MoS_2/MoO_x heterostructures exhibit enhanced visible–light photocatalytic activity and good compatibility in a wide range of PH values (e.g. 2–12) for degradation of organic dyes, both of which are of significance for practical applications. The vertically grown nanosheets forming a three–dimensional (3D) mesh structure create the large specific surface area for the optical absorption and the catalytic redox reaction. Particularly, the sulfidization–produced MoS_2 coating layer provides an effective protective against photocorrosion in wide PH window, meanwhile modulating energy band structure to promote the absorption of visible–light photons and the separation of photo–generated electron–hole pairs.

Introduction

With the energy crisis and the environmental pollution increasing, the semiconductor–based photocatalytic technology has been widely utilized in the fields of solar energy conversion and wastewater treatment.[1–3] Especially, TiO_2 as a leading representative has exhibited the inspiring potential for photocatalytic hydrogen evolution and dye degradation.[4,5] However, the wide band gap (> 3.2 eV) of TiO_2 limits greatly its utilization of the visible light dominating in the solar spectrum, thus it is highly desirable to develop alternative photocatalysts with high catalytic activities under the visible light.[6,7] Recently, on the basis of energy band engineering, the ingenious configuration of semiconductor heterostructures have been demonstrated be an effective approach to harvest more visible light and promote charge separation, leading to the improved photocatalytic activity under the visible light.[8–10] Noteworthy, molybdenum (Mo) oxides and sulfides have invoked increasing research interest as the promising electrocatalysts and photocatalysts even photoelectrocatalysts for versatile applications in environmental and energy issues.[11–13] Molybdemum oxides like MoO_2 and MoO_3 are well–studied semiconductors with superior properties and are extensively used as active materials in photoelectrocatalysis, sensors, supercapacitors and lithium ion batteries.[11] In particular, few–layered MoS_2 with many unique optical properties, such as layer–modulated narrow band gap,[14] strong light-matter interaction[15] and anti–photo corrosion,[16] has been illustrated as a superior co-catalyst for visible–light–driven photocatalysis in some nanocomposites like

CdS/MoS_2,[17] TiO_2/MoS_2[18] and g–C_3N_4/MoS_2,[19] etc, opening up new avenues for solar photocatalytic water splitting and wastewater treatment. Although the MoO_3– and MoS_2–based heterojunction photocatalysts with improved photocatalytic activities were frequently reported in recent years,[18–21] to the best of our knowledge, Mo oxide/sulfide heterostructure has been rarely constructed to explore their photocatalytic performance so far. However, Mo oxide and sulfide share the same cation, endowing their forming heterostructure with an intimate heterojunction interface, which has been demonstrated in the core–shell MoO_3/MoS_2 nanowire heterostructure as an excellent electrocatalyst for hydrogen evolution.[22]

Herein, we designed the vertically oriented core–shell nanosheets with polycrystalline MoO_x cores and conformal MoS_2 shells by sulfidizing MoO_3 templates to achieve some promising advantages as the following: (ⅰ) the mesh-shaped morphology composing of the vertically standing nanosheets to enable higher specific surface area, (ⅱ) the location of large–area and uniform photocatalyst on a transparent substrate to realize convenient separation of catalyst and avoid the secondary pollution, (ⅲ) the matched energy band formed by coupling between Mo oxide and sulfide to capture more solar photons and to promote the charge separation, (ⅳ) the surface coverage of few–layered MoS_2 with abundant active edge sites, anti–photo corrosion and chemical stability in wide PH window to improve the catalytic activity and provide a protection against photocorrosion. As a proof of concept, we demonstrated that the as–synthesized MoS_2/MoO_x heterojunction

nanosheets are an excellent photocatalyst for the visible–light–driven degradation of organic dyes, e.g. Rhodamine B (RhB).

Experimental

Synthesis of MoO_3 nanosheets. The MoO_3 nanosheets were prepared by chemical vapor deposition (CVD) method, as illustrated schematically in Fig. S1(a) (Supporting Information). Typically, MoS_2 powder of 0.2 g as a source material was placed in a ceramic boat, which was inserted into the middle of the small quartz tube inside a horizontal tube furnace. A cleaned quartz substrate was horizontally put downstream of MoS_2 powder at a distance of 15 cm. Before heating, the system was purged with 517 sccm (standard cubic centimeter per minute) high–purity argon (Ar 99.999%) and high–purity oxygen (O_2 99.999%) for 20 min. Then, the pressure was reduced to 7.5×10^{-2} Torr for the duration of the reaction. After that, the furnace was heated by the heating rate of 10 ℃/min to the temperature of 900 ℃ and kept at the temperature for 20 min with the Ar flow of 26 sccm and the O_2 flow of 4 sccm. After the system was cooled down to room temperature, bluish white–colored product like wool was found deposited onto the quartz substrate.

Synthesis of MoS_2/MoO_x (MSO) heterostructures. MoS_2/MoO_x (MSO) composited nanosheets were synthesized via a CVD sulfurization of as–obtained MoO_3 nanosheets in sulphur atmosphere, as illustrated schematically in Fig. S1(b) (Supporting Information). Typically, S powder of 0.8 g was placed in the center of the heating zone of a tube furnace. The quartz substrate coated with MoO_3 nanosheets

was horizontally put downstream of S powder at a distance of 8 cm. Before heating, the system was purged with 517 sccm high–purity argon (Ar 99.999%) for 30 min. Then, the pressure was reduced to 7.5×10^{-2} Torr for the duration of the reaction. After that, the furnace was heated by the heating rate of 10 ℃/min to the certain temperatures of 600, 700 and 800 ℃, respectively, then the temperature was kept for 10 min with the Ar flow of 10 sccm. Obviously, such a sulfidization changes the color of the samples from original bluish white to ink black, as shown in the photographs of samples before and after the sulfidization (Fig. S2 in Supporting Information). We determined the temperature of sulfidization as a key parameter that controls the phase transition of MoO_3, as well as the formation and thickness of MoS_2 coverage. As the representative samples, the heterojunction nanosheets formed at different sulfidization temperatures of 600, 700 and 800 ℃ were labeled as MSO1, MSO2, MSO3, respectively.

Characterization of MSO heterostructures. The as-synthesized samples were characterized by X–ray diffraction (XRD–7000, Shimadzu) using Cu Kα radiation (λ = 0.15406 nm). The morphologies were observed using a field emission scanning electron microscopy (FESEM, Hitachi, S–4800II), and a high–resolution transmission electron microscope (HRTEM, Tecnai F30, FE) equipped with X–ray energy dispersive spectrum (EDS), respectively. The diffuse reflectance absorption spectra (DRAS) of the samples were recorded by an UV−vis spectrophotometer (Varian Cary 5000) in the range from 200 to 800 nm equipped with the pure quartz as a reference.

The Raman spectra were collected using an excitation wavelength of 532 nm and an incident laser light power of 300 mW in Renishaw In Via equipment.

Photocatalytic activity tests. Five different materials including pure MoO_3 nanosheets, MSO heterostructures with different sulfidization extent (MSO1, MSO2 and MSO3) and commercial P25 TiO_2 were respectively put in the weighing bottle containing 8 mL of 0.4×10^{-5} mol/L (about 191.6×10^{-5} g/L) of RhB aqueous solution to examine their photocatalytic activities under the visible light of wavelength longer than 420 nm. The light irradiation was from a 300 W xenon lamp with a 420 nm cutoff filter ($\lambda > 420$ nm, GHX–2 Photochemical Reactions Instrument, Yangzhou University City Science and Technology Co., Ltd). During the illumination process, about 5 mL of RhB aqueous solution was taken out at an interval of 30 min. The dye degradation process was recorded by monitoring the concentration changes of RhB at its typical absorption wavelength of 553 nm, using the JH 722S Vis spectrophotometer. Then the extracted RhB solution was removed to the weighing bottle for the continued photocatalytic degradation. We also investigated the recyclability the MSO1 with the best photocatalytic activity and its environmental compatibility under the wide window of pH values from 2 to 13, where the pH values of RhB solutions were adjusted by adding HCl and NaOH.

Result and discussion

Figs. 1a–d show respectively the SEM images of MoO_3, MSO1, MSO2, and MSO3 before and after the sulfidization at different temperatures. Fig. 1(a) reveals that the

as–prepared MoO_3 nanosheets uniformly stand on the substrate, forming the three–dimension (3D) mesh–shaped structure with high specific surface area. Moreover, there are no noticeable differences in the overall morphology for these four samples before and after the sulfidization. However, it is worth noting that the sulfurizing treatment induces the wrinkle–like features from the smooth surface of original nanosheets, as shown in the amplifed SEM images of unsulfidized MoO_3 nansheets and MSO nansheets sulfidized at 600, 700 and 800 ℃ in the insets of Fig. 1. Furthermore, with the sulfidizing temperature increasing, such a wrinkle–like surface feature is more intense, indicating observably an increase in sulfidization degree under the control of temperature.

In order to know further the microstructural change induced by the sulfidization, the TEM and HRTEM of samples before and after the sulfidization are compared in Figs. 2(a)–(d). Figs. 2(a) and (c) show respectively the typical TEM images of an individual nanosheet before and after the sulfidization of 600 ℃. It can be seen clearly that the additional layers appear at the edge of nanosheet after the sulfidization, revealing a coverage–forming core–shell heterostructure. In addition, the corresponding EDS spectra acquired from the whole area of these two samples, as shown in Fig. S3 in the Supporting Information, suggests that the incorporated of S element into the stoichiometric Mo–O NSs after the sulfidization, and some other detected elements including Fe and Cu are derived from the Cu mesh braces. The line–sweeping EDS spectra acquired from the surface and edge areas are shown in Fig.

S4 in the Supporting Information, revealing the formation of Mo–sulfide coating. Especially, the line–sweeping EDS spectra of S, Mo and O elements along with the marked arrow direction perpendicular to the nanosheet edge illustrate that the covering shell is composed mainly of Mo and S atoms with an approximate proportion of 1 : 2, as shown in the inset in the lower–left corner of Fig. 2c. Moreover, in Figs. 2(b) and (d), the HRTEM images acquired from the edge regions of these two nanosheets show that the as-synthesized MoO_3 nanosheet is almost single (110) crystal with a lattice spacing of 0.375 nm, whereas the sulfidized MSO1 nanosheet exhibits the interlayer (002) plane of MoS_2 with lattice spacing of 0.62 nm, and the (011) with lattice spacing of 0.347 nm and (020) plane with lattice spacing of 0.245 nm of MoO_2, confirming further the integration the conformal MoS_2 and the substoichiometric MoO_x. According to the previous studies,[22,23] it is reasonable for the formation of MoO_2 as a transition state during the sulfidization reduction process, i. e. that the MoO_3 nanosheets was reduced firstly at their surfaces by the sulfur vapor to form suboxide MoO_2 which then reacted with sulfur vapor to grow layered MoS_2 shells.

Such a dynamic process of sulfidization can be further supported by analysing the evolution of XRD patterns shown in Fig. 3. The diffraction peaks (*) of unsulfidized nanosheets match the standard phases of orthorhombic α–MoO_3 with lattice constants a = 0.3962 nm, b = 1.3858 nm, and c = 0.3697 nm (JCPDS card no. 05–0508). For the MSO heterostructures sulfidized at 600, 700 and 800 ℃, all peaks associated to

MoO_3 disappear, while the detected peaks can be indexed respectively to the hexagonal phase MoS_2 (+) (JCPDS card no. 37–1492) and the monoclinic MoO_2 phase (#) (JCPDS card no. 65–5787), indicating the crystallization of Mo^{4+} oxide and sulfide displacing the original MoO_3 phase in the near-surface region detected by X–ray irradiation. Moreover, the intensity of (002) peak at 14.5° corresponding to the *c*–plane of MoS_2 becomes relatively higher with the increase of sulfidization temperature, which reveals that the higher temperature induces the thicker MoS_2 coating, consistent with the SEM images in Fig. 1, demonstrating further the sulfidizing dynamics mentioned above.

The Raman spectra were used to verify further the chemical composition of samples before and after the sulfidization, as shown in Fig. 4. For the unsulfidized sample, all vibration peaks (*) are in good agreement with those reported in literature for the orthorhombic α–MoO_3 crystalline phase.[24] Typically, in the region between 600 and 1000 cm^{-1}, the three peaks at 666, 819 and 996 cm^{-1} are assigned to the stretching modes resulting from the triply coordinated oxygen (Mo—$O_{(3)}$), the doubly coordinated oxygen (Mo—O—Mo) and the terminal oxygen (Mo=O). After the sulfidization, the two characteristic Raman peaks (+) at 379 and 405 cm^{-1} of MoS_2 emerge,[25] which are associated with the E^1_{2g} (in-plane vibration of two S atoms with respect to the Mo atom) and A_{1g} (out–of–plane vibration of S atoms) modes, moreover, the intensities of these two peaks increase with the increase of sulfidization temperature. In addition, in the range of 480–800 cm^{-1}, the three peaks (#) at 726,

571 and 486 cm^{-1} induced by the sulfidization are in good agreement with that reported for monoclinic MoO_2.[26] The analyses of Raman spectra indicate further that the temperature–dependent sulfidization can drive the reduction reaction of Mo^{6+} oxide into Mo^{4+} oxide and sulfide in the near–surface region of MoO_3 to form the core–shell composited nanosheets, and can modulate the thickness of MoS_2 coating. Meanwhile, noting that the existence of suboxide MoO_2 with low electrical resistivity may enable the facile carrier transport, being conducive to the separation of photogenerated electron–hole pairs at the heterojunction interface.

Fig. 5 shows the UV–vis absorbance spectra of MoO_3, MSO1, MSO2 and MSO3 samples before and after the sulfidization. For the pure MoO_3 nanosheets, a strong absorption at wavelength shorter than 415 nm can be attributed to the intrinsic band gap of $E_g \approx 3.0$ eV. After the layered MoS_2 coating on the MoO_3 nanosheets, the light absorption in the visible–light region is significantly extended and is enhanced with the sulfidization extent increasing. For the MoS_2 with the layer–dependent band gap (1.2−1.8 eV),[27] there is usually showing a strong absorption feature above the fundamental band gap because of the strong dipole transition between localized d orbits and the band nesting enhanced by van Hove singularities in the electronic state density.[28–30] Specifically, the characteristic A and B excitonic peaks between 500 and 700 nm arising from the direct excitonic transitions with the energy split from pin–orbital coupling in valence bands at the Brillouin zone K point are observed in the MSO1 sample,[18,31] confirming the absorbing contribution of few–layered MoS_2 shells.

Moreover, the few–layered MoS_2 with an indirect band gap has the multipeak-absorption feature above the fundamental band gap and can restraint the direct recombination of electron−hole pairs. Therefore, the layered MoS_2 coating serves as the visible–light absorber, simultaneously promoting the separation of photo–excited electrons and holes.

As a proof–of–concept application, we use respectively MoO_3, MSO1, MSO2 and MSO3 as the photocatalysts for degrading RhB dye to examine their photocatalytic activities under the visible–light irradiation (λ > 420 nm). Fig. 6(a) compares the time–dependent degradation curves of aforementioned samples as well as the black sample (without catalyst) and commercial P25 TiO_2 as two references. The measured absorbance intensities of RhB dye at its typical wavelength of 553 nm with the illumination time were recorded in Table S1 in the Supporting Information then transformed to the RhB degradation ratio (η) according to the following equation: $\eta = (1 - C / C_0) \times 100\%$, where C_0 and C are respectively the initial concentration and the actual concentration of RhB at different irradiation time, thus the lower C / C_0 denotes the higher degradation degree of the RhB dye. As shown in Fig. 6(a), the RhB hardly shows the self–degradation ($\eta \approx 2\%$), while both the pure MoO_3 nanosheets and the commercial P25 TiO_2 exhibit the slight degradation ($\eta \approx 48\%$ and 41%, respectively) after 120 min of visible–light irradiation. In contrast, the sulfidized samples (MSO1, MSO2 and MSO3) perform the obviously enhanced photocatalytic efficiency, and the slightly sulfidized MSO1 as among the best brings out a superior

degradation ratio ($\eta \approx 97\%$) after 120 min of visible–light irradiation. To quantitatively evaluate the photocatalytic activities of these catalysts, the corresponding apparent reaction rate constants (k) of the RhB degradation were calculated by using an equation $\ln(C_0 / C) = kt$ based on the pseudo-first-order kinetic model, which are compared in Fig. 6b. For the blank experiment (without catalysts), the RhB degrades at relatively slow reaction rate with $k = 1.61\times10^{-4}$ min^{-1}. For other catalysts (P25 TiO_2, MoO_3, MSO1, MSO2 and MSO3), the corresponding degradation rates with $k = 4.43\times10^{-4}$, 5.58×10^{-3}, 2.81×10^{-2}, 2.26×10^{-2} and 2.05×10^{-2} min^{-1} were obtained respectively, and MSO1 shows the prominent photocatalytic activity. Obviously, such a significant increase in photocatalytic activity results certainly from the integration of MoS_2, however, the extra coverage of MoS_2 can lower instead the photocatalytic activitiy, which may be due to that the excessively thick MoS_2 covering can hinder the penetration of the incident light and the carrier transport to produce more nonradiative phonons (heat), thereby reducing the photocatalytic efficiency.

To examine the practical value in wastewater treatments, we studied the compatibility to PH values and the reusability of MSO1 for the photocatalytic degradation of RhB dye. As shown in Fig. 7(a), the degradation efficiency of MSO1 remains almost unchanged in acidic media with the PH value range of 2–7, and it decreases slightly in alkaline media with the PH value increasing from 7 to 12. Noting that for the stable photocatalytic activity, the PH-compatibility window of MSO1 is

much wider than that of MoO_3, revealing the protective action of MoS_2 shells against photocorrosion in a wide PH window. Fig. 7(b) shows the reusability of MSO1 for another four cycles of photocatalytic degradation of RhB dye. No significant loss of activity indicates that the MSO1 can keep stable recyclability in the process of photocatalytic degradation of RhB dye. The measured absorbance intensities of RhB dye at its typical wavelength of 553 nm with the illumination time were recorded respectively for different PH values and for four sequential cycles (Tables S2 and S3 in the Supporting Information).

Based on the above investigation, the enhanced photocatalytic activity and stability must result from the synergetic effect in the core–shell MoS_2/MoO_3 heterostructure with conductive MoO_2 component at their interface. Such a unique nanocomposite allows integration of the advantages from different materials, i.e. the few–layered MoS_2 shell can harvest more visible light, simultaneously can provide a protection against photocorrosion in the wide PH window; the MoO_2 with high conductivity can enable carrier transport at interfaces; the MoO_3 core with a wide band gap can absorb the near–ultraviolet photons to accrue the active charges. In particular, a tandem band–gap structure with band bending is formed at the heterojunction interface, as illustrated schematically in Fig. 8. The band positions of MoO_3 and MoS_2 could be estimated by the following empirical formulas: $E_C = \varepsilon - E_H - 0.5E_g$ and $E_B = E_C + E_g$, where ε is the absolute electronegativity of atom semiconductor, which is defined as the arithmetic mean of the atomic electro affinity and the first

ionization energy; E_H is the energy of free electrons of hydrogen scale (4.5 eV); E_C and E_B are respectively the potentials of conduction and valance bands, and E_g is the band gap between the conduction and valance bands. According to the above equations, the conduction band potentials of MoO_3 and MoS_2 were calculated to be 0.44 and 0.4 eV similar to the previous reports,[17,32] then their valance band potentials were deduced to be about 3.36 and 2.3 eV. Therefore, the reverse transporting of positive and negative charge carriers across the MoS_2 /MoO_3 interface could drive the separation of photogenerated electron–hole pairs to retard their radiative recombination and nonradiative relaxation (phonon heat), prolonging the carrier lifetime. The photo–excited electrons converge on the conduction band of MoO_3 core and reduce the absorbed oxygen molecules on MoO_3 surface, inducing the chain reactions as following: $e^- + O_2 \rightarrow O_2^{\bullet -}$, $O_2^{\bullet -} + H^+ \rightarrow HO_2^{\bullet}$, $HO_2^{\bullet} + e^- \rightarrow H_2O_2$, and $H_2O_2 + e^- \rightarrow \bullet OH$, thus which produce the strongly oxidizing hydroxyl radicals ($\bullet OH$). Meanwhile, the photo–excited holes flock to the valance band of MoS_2 shell and react with adsorbed water and OH^- to produce more $\bullet OH$ via the reaction: $hole^+ + H_2O / OH^- \rightarrow \bullet OH + H^+$. Subsequently, these strongly oxidising $\bullet OH$ species could degrade the RhB dye into some small molecules like CO_2 and H_2O, etc. via the reaction: $RhB + \bullet OH \rightarrow CO_2 + H_2O + NO_3^- + NH_4^+ + Cl^-$.

Conclusions

The vertically standing MoS_2/MoO_x nanosheet heterostructures were successfully synthesized by a facile two–step CVD route. The results demonstrate the creative

construction of wide bandgap MoO_3 core and narrow bandgap MoS_2 shell with conductive MoO_2 heterointerface, where they have the synergistic effect on the collection of visible–light–generated charge carriers. Thus a significantly enhanced photocatalytic activity was achieved in MoS_2/MoO_x heterostructure relative to pure MoO_3, which could be attributed to the dual functions resulting from the connection of few–layered MoS_2, that are both the extended utilization of visible light and the formation of matched energy band for charge separation. In addition, the MoS_2 coating also serves as a protection layer against photocorrosion, maintaining the stability and recyclability of MoS_2/MoO_x photocatalyst for degrading organic dye in wide PH-compatibility window. This work indicates the promising potential of core–shell MoS_2/MoO_x heterostructures as visible–light photocatalyst in application fields of photodegrading contaminants and photocatalytic energy conversion.

Supporting information

Schematic illustration for the synthesis of MSO heterostructures by the two–step CVD route, Digital photographs of MoO_3 and MSO1, Schematic illustration for the construction of MSO, EDS spectra of MoO_3 and MSO1, The line–sweeping EDS spectra acquired from the edge and the surface areas of MSO1, The absorbance intensities of RhB aqueous solution at its typical wavelength of 553 nm with the illumination time for different photocatalysts, The absorbance intensities of RhB aqueous solution with the illumination time at different PH values for MoO_3 and MSO1, as well as the absorbance intensities of RhB aqueous solution (after the

illumination of 120 min) in five sequential recycles for MSO1. This material is available free of charge via the Internet at http://pubs.acs.org.

Acknowledgments

This work was supported by the National Natural Science Foundation of China (Grants 11104240 and 11374253) and the Innovation Projects in 2014 (Grants 120801112 and 120804123). And we thank the Testing Center of Yangzhou University for the technical supports.

References

1 P. Lianos, *J. Hazard. Mater.*, 2011, **185**, 575.

2 M. N. Chong, B. Jin, C. W. K. Chow and C. Saint, *Water Res.*, 2010, **44**, 2997.

3 Y. Yang, G. Z.Wang, Q. Deng, S. H. Kang, D. H. L. Ng and H. J. Zhao, *CrystEngComm*, 2014, **16**, 3091..

4 N. Q. Wu, J. Wang, D. N. Tafen, H. Wang, J. G. Zheng, J. P. Lewis, X. G. Liu, S. S. Leonard and A. Manivannan, *J. Am. Chem. Soc.*, 2010, **132**,6679.

5 T. Fröschl, U. Hörmann, P. Kubiak, G. Kučerová, M. Pfanzelt, C. K. Weiss, R. J. Behm, N. Hüsing, U. Kaiser, K. Landfester and M. Wohlfahrt–Mehrens, *Chem. Soc. Rev.*, 2012, **41**, 5313.

6 C. H. Li, T. Ming, J. X. Wang, J. F. Wang, J. C. Yu and S. H. Yu, *J. Catal.*, 2014, **310**, 84.

7 Y. C. Zhang, J. Li, M. Zhang and D. D. Dionysiou, *Environ. Sci. Technol.*, 2011, **45**, 9324.

8 J. Zhang, Z. P. Zhu, Y. P. Tang, K. Müllen and X. L. Feng, *Adv. Mater.*, 2013, **26**, 734.

9 S. D. Zhuang, X. Y. Xu, B. Feng, J. G. Hu, Y. R. Pang, G. Zhou, L. Tong and Y. X. Zhou, *ACS Appl. Mater. Interfaces*, 2014, **6**, 613.

10 Z. Y. Yin, Z. Wang, Y. P. Du, X. Y. Qi, Y. Z. Huang, C. Xue and H. Zhang, *Adv. Mater.*, 2012, **24**, 5374.

11 Y. F. Zhao, Y. X. Zhang, Z. Y. Yang, Y. M. Yan and K. N. Sun, *Adv. Mater.*, 2013, **14**, 043501.

12 U. Maitra, U. Gupta, M. De, R. Datta, A. Govindaraj and C. N. R. Rao, *Angew. Chem. Int. Ed.*, 2013, **52**, 1.

13 Y. P. Chen, G. Yang, Z. H. Zhang, X. Y. Yang, W. H. Hou and J. J. Zhu, *CrystEngComm*, 2010, **12**, 3740.

14 H. S. Lee, S. W. Min, Y. G. Chang, M. K. Park, T. Nam, H. Kim, J. H. Kim, S. Ryu and S. Im, *Nano Lett.*, 2012, **12**, 3695.

15 G. Eda and S. A. Maier, *ACS Nano*, 2013, **7**, 5660.

16 Y. L. Min, G. Q. He, Q. J. Xu and Y. C. Chen, *J. Mater. Chem. A*, 2014, **2**, 2578.

17 Y. Liu, Y. X. Yu and W. D. Zhang, *J. Phys. Chem. C*, 2013, **117**, 12949.

18 W. J. Zhou, Z. Y. Yin, Y. P. Du, X. Huang, Z. Y. Zeng, Z. X. Fan, H. Liu, J. Y. Wang and H. Zhang, *Small*, 2013, **9**, 140.

19 L. Ge, C. C. Han, X. L. Xiao and L. L. Guo, *Int. J. Hydrogen Energy*, 2013, **38**, 6960.

20 X. F. Song, J. L. Hu and H. B. Zeng, *J. Mater. Chem. C* 2013, **1**, 2952.

21 T. Jia, A. Kolpin, C. Ma, R. C. T. Chan, W. M. Kwokc and S. C. E. Tsang, *Chem. Commun.*, 2014, **50**, 1185.

22 Z. B. Chen, D. Cummins, B. N. Reinecke, E. Clark, K. S. Mahendra and F. J. Thomas, *Nano Lett.*, 2011, **11**, 4168.

23 Y. H. Lee, X. Q. Zhang, W. J. Zhang, M. T. Chang, C. T. Lin, K. D. Chang, Y. C. Yu, J. T. W. Wang, C. S. Chang, L. J. Li and T. W. Lin, *Adv. Mater.*, 2012, **24**, 2320.

24 Z. Y. Shen, G. Chen, Y. G. Yu, Q. Wang and C. Zhou, *J. Mater. Chem.*, 2012, **22**, 19646.

25 B. Radisavljevic, A. Radenovic, J. Brivio, V. Giacometti and A. Kis, *Nat. Nanotech.*, 2011, **6**, 147.

26 W. Luo, X. L. Hu, Y. M. Sun and Y. H. Huang, *Phys. Chem. Chem. Phys.*, 2011, **13**, 16735.

27 K. F. Mak, C. Lee, J. Hone, J. Shan and T. F. Heinz, *Phys. Rev. Lett.*, 2010, **105**, 136805.

28 A. Carvalho, R. M. Ribeiro and A. H. C. Neto, *Phys. Rev. B*, 2013, **88**, 115205.

29 M. Bernardi, M. Palummo and J. C. Grossman, *Nano Lett.*, 2013, **13**, 3664.

30 G. Eda, H. Yamaguchi, D. Voiry, T. Fujita, M. Chen and M. Chhowalla, *Nano Lett.*, 2011, **11**, 5111.

31 A. Splendiani, L. Sun, Y. B. Zhang, T. S. Li, J. Kim, C. Y. Chim, G. Galli and F. Wang, *Nano Lett.*, 2010, **10**, 1271.

32 S. H. Elder, F. M. Cot, Y. Su, S. M. Heald, A. M. Tyryshkin, M. K. Bowman, Y. Gao, A. G. Joly, M. L. Balmer, A. C. Kolwaite, K. A. Magrini and D. M. Blake, *J. Am. Chem. Soc.*, 2000, **122**, 5138.

Figure Captions

Fig. 1 SEM images of (a) unsulfidized MoO_3, and (b) MSO1, (c) MSO2 and (d) MSO3 sulfidized at different temperatures of 600, 700 and 800 ℃. The insets show their amplified SEM images, respectively.

Fig. 2 TEM and HRTEM images of (a, b) unsulfidized MoO_3 and (c, d) MSO1 sulfidized at 600 ℃. The insets in the top−left corners of (a) and (c) show the TEM images of their individual nanosheets, respectively. The inset in the lower−left corner of (c) shows the line−sweeping EDS spectra of S, Mo and O elements along with the marked arrow direction perpendicular to the MSO1 nanosheet edge.

Fig. 3 XRD patterns of unsulfidized MoO_3, and (b) MSO1, (c) MSO2 and (d) MSO3 sulfidized at different temperatures of 600, 700 and 800 ℃ with the corresponding characteristic peaks: MoO_3 (*), MoO_2 (#), and MoS_2 (+).

Fig. 4 Raman patterns of unsulfidized MoO_3, and (b) MSO1, (c) MSO2 and (d) MSO3 sulfidized at different temperatures of 600, 700 and 800 ℃ with the corresponding characteristic peaks: MoO_3 (*), MoO_2 (#), and MoS_2 (+).

Fig. 5 UV−vis absorption spectra of unsulfidized MoO_3, and (b) MSO1, (c) MSO2 and (d) MSO3 sulfidized at different temperatures of 600, 700 and 800 ℃.

Fig. 6 (a) Degradation curves and (b) apparent reaction rate constants (*k*) of the RhB aqueous solutions with PH value of 7 under the visible−light irradiation for different photocatalysts: Blank sample (without catalyst), MoO_3, MSO1, MSO2 and MSO3.

Fig. 7 (a) Photocatalytic efficiencies of MoO_3 and MSO1 at different pH values from 2 to 12. (b) Photocatalytic efficiencies of MSO1 in five sequential recycles.

Fig. 8 Schematic illustration of the dynamic process of photogenerated carriers in the matched energy−band structure at MoS_2/MoO_x heterointerface under the visible−light irradiation ($\lambda > 420$ nm).

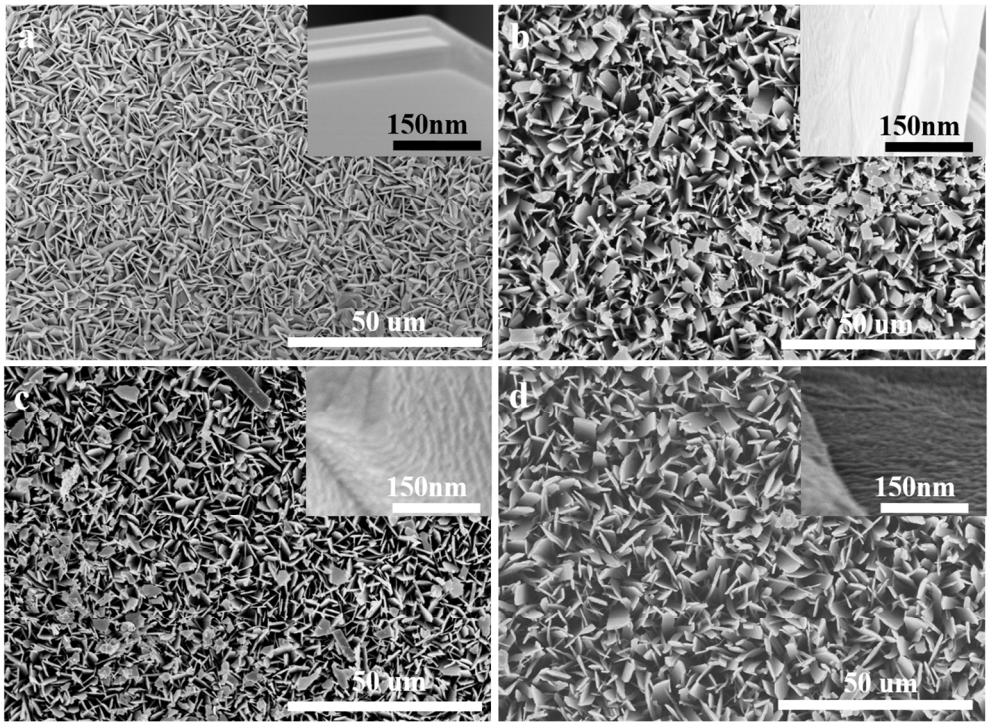

353x254mm (96 x 96 DPI)

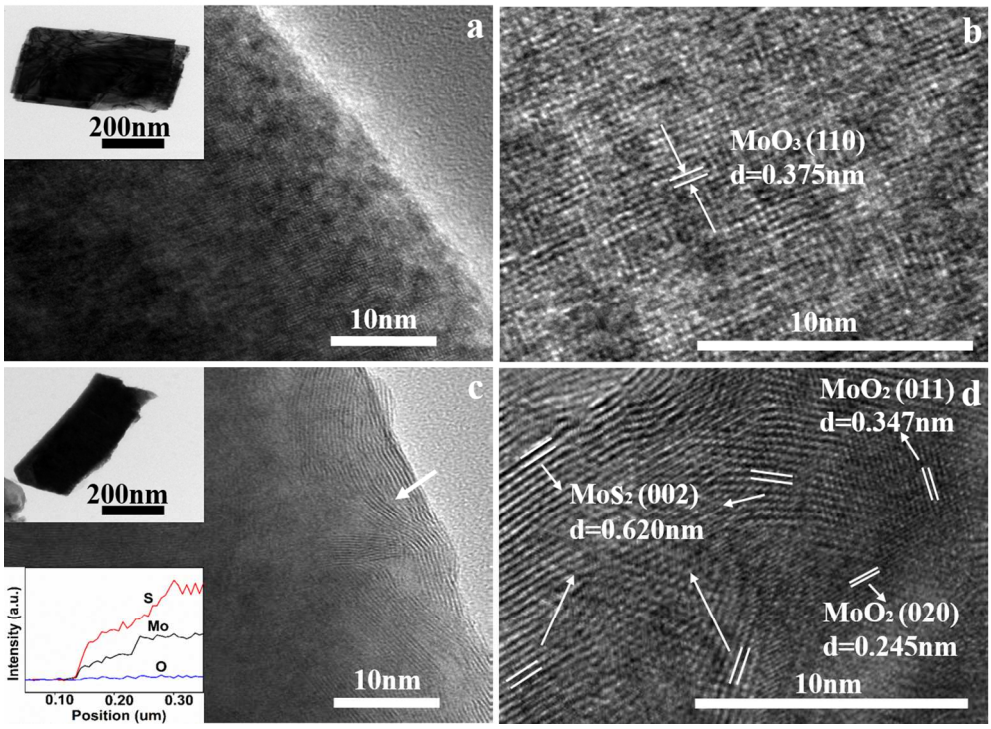

352x258mm (96 x 96 DPI)

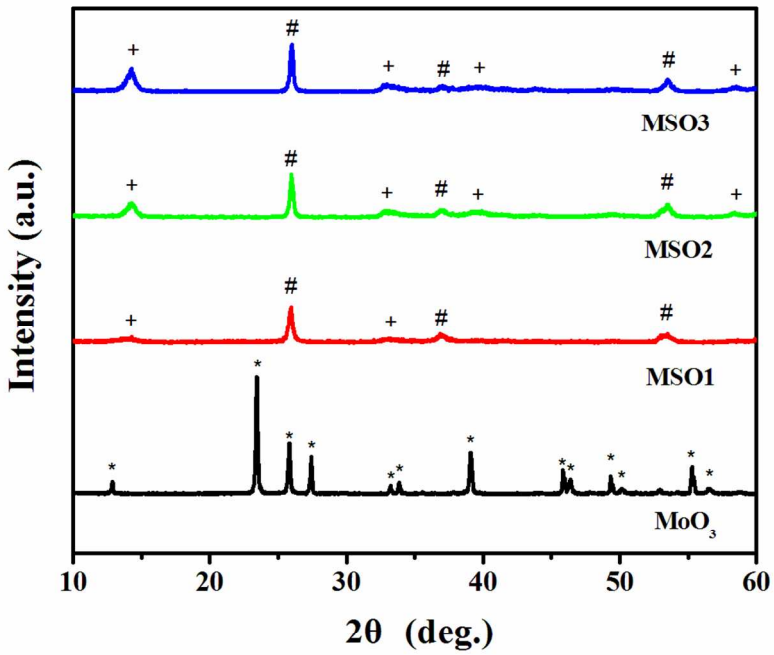

219x180mm (150 x 150 DPI)

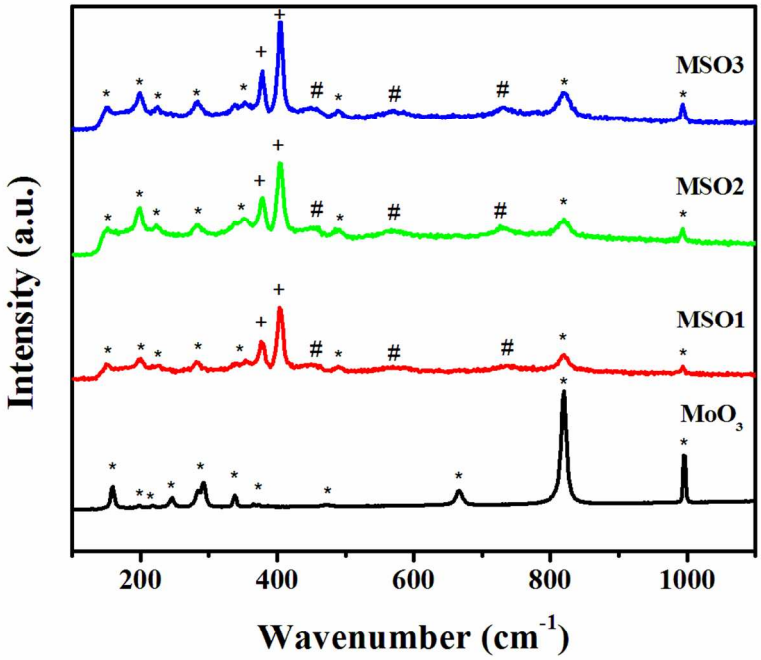

219x180mm (150 x 150 DPI)

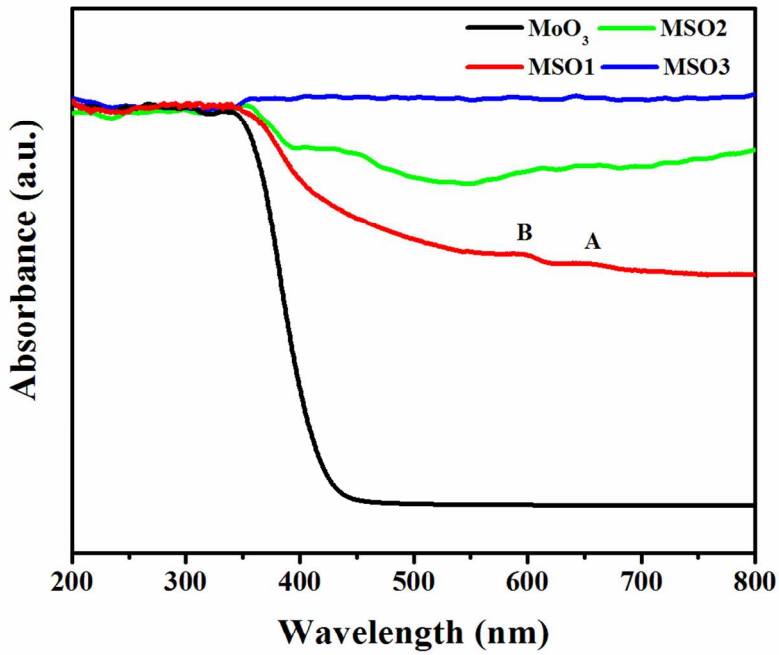

219x179mm (150 x 150 DPI)

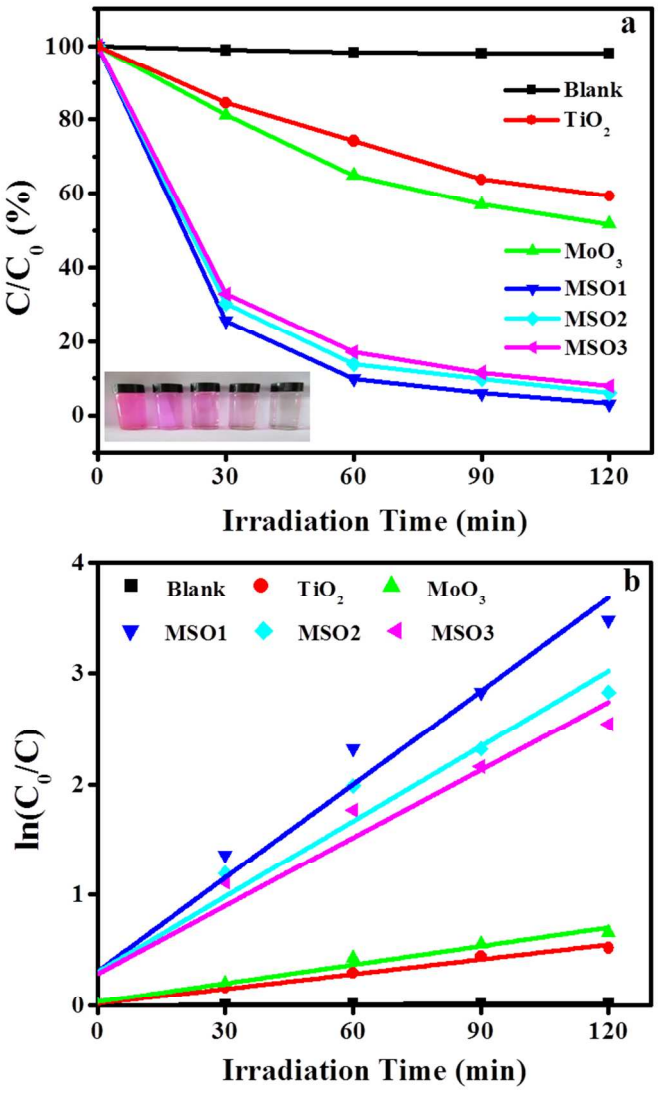

234x364mm (96 x 96 DPI)

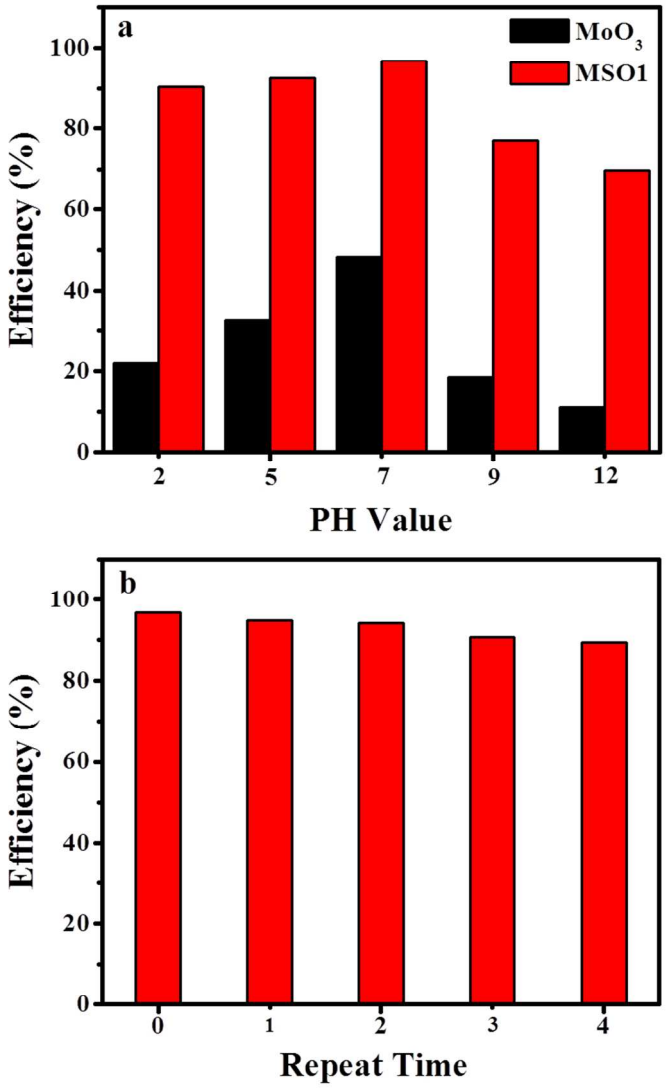

234x361mm (96 x 96 DPI)

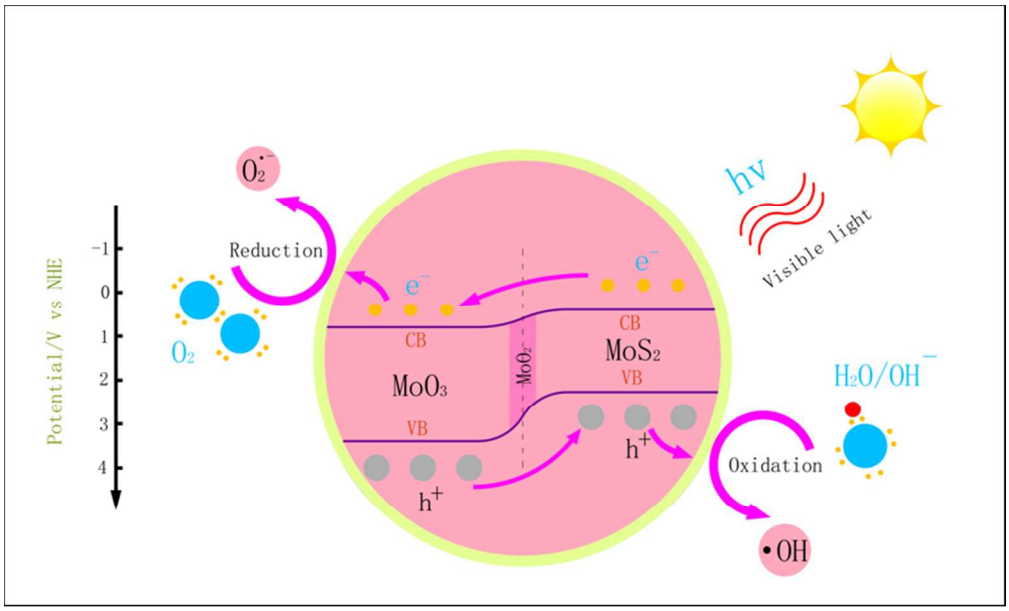

150x90mm (150 x 150 DPI)